

1  
2  
3  
4  
5  
6  
7  
8  
9  
10  
11  
12  
13  
14  
15  
16

# **Revisited heat budget and probability distributions of turbulent heat fluxes in the Mediterranean Sea**

Mahmud Hasan Ghani<sup>1</sup>, Nadia Pinardi<sup>1,2</sup>, Antonio Navarra<sup>2,3</sup>, Lorenzo Mentaschi<sup>1,2</sup>,  
Silvia Bianconcini<sup>4</sup>, Francesco Maicu<sup>2</sup>, and Francesco Trotta<sup>2</sup>

<sup>1</sup> Dept. of Physics and Astronomy, University of Bologna, Bologna, Italy  
<sup>2</sup> CMCC Foundation - Euro-Mediterranean Center on Climate Change, Italy  
<sup>3</sup> Dept. of Biological, Geological and Environmental Sciences, University of Bologna, Bologna, Italy  
<sup>4</sup> Dept. of Statistics, University of Bologna, Bologna, Italy

*Corresponding author:* Mahmud Hasan Ghani, [mahmudhasan.ghani2@unibo.it](mailto:mahmudhasan.ghani2@unibo.it)

## Abstract

17  
18  
19 Understanding the surface heat budget of the Mediterranean Sea is essential for assessing its role in regional climate  
20 and ocean circulation. Under the steady-state heat budget closure hypothesis, the Mediterranean should exhibit a  
21 net surface heat loss to balance the heat gained through the inflow of warm Atlantic water at the Gibraltar Strait.  
22 However, literature estimates of the net heat flux vary widely, raising questions about the accuracy of existing  
23 reanalysis products. In this study, we compute the net surface heat flux over the Mediterranean using two  
24 atmospheric datasets: high-resolution ( $0.125^\circ$ ) ECMWF analysis and lower-resolution ( $0.25^\circ$ ) ERA5 reanalysis. By  
25 applying the same sea surface temperature fields and bulk formulas in both cases, we isolate the impact of  
26 atmospheric resolution and data quality. We find that the ECMWF analysis yields a basin-averaged net heat flux  
27 of  $-3.6 \pm 1.3 \text{ W m}^{-2}$ , consistent with the closure hypothesis, while ERA5 gives a spurious positive flux of  
28  $+5 \pm 1.2 \text{ W m}^{-2}$ . Furthermore, beyond simply assessing the net heat budget, this study delves into the probability  
29 distributions of air-sea heat fluxes, aiming to gain a deeper understanding of associated uncertainties and extreme  
30 values in turbulent heat fluxes. The probability distributions for turbulent heat flux components exhibit  
31 characteristics such as skewness and kurtosis, respectively, varying across the basin. To assess the influence of  
32 extremes, we apply the Interquartile Range (IQR) method within statistical models that account for the skewed  
33 nature of turbulent heat flux distributions, enabling a consistent treatment of outliers. Our results reveal that extreme  
34 negative heat flux events play a critical role in determining the net heat flux direction; excluding these extremes  
35 leads to a spurious positive heat budget. Only ECMWF fields are consistent with the heat budget closure hypothesis.  
36 Furthermore, we demonstrate that the Mediterranean heat budget closure hypothesis is connected to extreme heat  
37 loss events occurring in key regions of the basin, such as the Gulf of Lion, the Adriatic Sea, the Aegean Sea, and  
38 the southern Turkish coasts.

39 KEYWORDS: Air-Sea Heat Fluxes, Heat Budget, Fluxes Probability Distributions, Extreme Heat Fluxes,  
40 Mediterranean Sea

41

42 **1. Introduction**  
43

44 The exchange of momentum, water, and heat between the atmosphere and ocean plays a pivotal role in connecting  
45 their dynamics (Kara et al., 2000). These fluxes, influenced by atmospheric surface variables and Sea Surface  
46 Temperature (SST), drive ocean circulation (Large and Yeager, 2009; Small et al., 2019).

47 Our study focuses on the Mediterranean Sea, a unique semi-enclosed anti-estuarine basin where heat, water, and  
48 momentum fluxes intertwine to fuel a robust vertical circulation (Pinardi et al., 2019). The Mediterranean heat  
49 budget comprises of two main terms- the basin averaged surface and lateral boundary heat fluxes. Large  
50 uncertainties are associated with surface heat fluxes at different temporal scales (Jorda' et al., 2017). We aim to  
51 reassess the long term mean net heat flux of the basin since this flux is a source of energy for the basin wide  
52 circulation (Cessi et al., 2014).

53 Understanding the heat budget in the Mediterranean Sea has long been a formidable task (Bignami et al., 1995;  
54 Castellari et al., 1998; Matsoukas et al., 2005; Pettenuzzo et al., 2010; Sanchez-Gomez et al., 2011; Criado-  
55 Aldeanueva et al., 2012; Jordà et al., 2017), whether through numerical models or observational data analysis. The  
56 fundamental challenge of in-situ observations is their limited spatial and temporal coverage, while numerical  
57 modelling is constrained by the semi-empirical nature of air-sea bulk formulas. Numerous endeavours have been  
58 undertaken (Large and Yeager, 2009) to calculate air-sea heat fluxes using atmospheric state variables obtained from  
59 in-situ observations, remote sensing data, or numerical model outputs. In this study, we utilize atmospheric analysis  
60 and reanalysis data, which provide an optimal reconstruction of past atmospheric surface state variables using  
61 models and observations. Furthermore, the estimate of the Mediterranean Sea heat budget from ECMWF  
62 meteorological analysis data sets has not been done before.

63 Numerous past studies have employed well-established bulk transfer formulas to estimate air-sea fluxes (e.g., Fairall  
64 et al., 2003; Pettenuzzo et al., 2010; Cronin et al., 2019). The turbulent heat flux components (latent and sensible  
65 heat flux) are commonly derived from surface wind speed, sea surface temperature, near-surface air temperature,  
66 and humidity (Large and Yeager, 2009). Gulev and Belyaev (2012) noted that global heat flux products often vary  
67 significantly, mainly due to differences in the bulk formulations and input variables adopted across studies.

68 At the Gibraltar Strait, the Mediterranean Sea exchanges water with the Atlantic through a characteristic two-layer  
69 flow: warm, relatively fresh Atlantic water enters at the surface, while colder, saltier Mediterranean water exits at  
70 depth leading to a net heat gain for the Mediterranean basin. To maintain a steady state balance in the basin averaged  
71 heat balance, this lateral heat gain must be compensated by a net loss of heat at the sea surface. In other words, the  
72 basin-average surface heat flux should be negative-a constraint known as the heat budget closure hypothesis.  
73 Accurately estimating this surface heat flux remains a challenge due to limited data and uncertainties in flux  
74 parameterizations. A benchmark estimates of the net heat budget,  $-7 \text{ W m}^{-2}$ , was proposed by Béthoux et al. (1998),  
75 though it is based on data from the 1970s and 1980s and may not reflect present-day conditions under a changing  
76 climate (Criado-Aldeanueva et al., 2012; Marullo et al., 2021). We realise that assuming perfect balance between  
77 lateral and vertical heat fluxes, even in the Mediterranean Sea, is an approximation. Being heat clearly entering the  
78 Mediterranean Sea through Gibraltar, we search for a negative net heat flux, which we call the closure hypothesis.

79 How negative such net heat flux is, we do not know but searching for a negative value is a conservative assumption  
80 aligned with current scientific understanding.

81 Recent studies highlight significant uncertainty in the estimated long-term net heat budget of the Mediterranean Sea,  
82 with some even reporting positive values. Song and Yu (2017), presented an ensemble climatology of surface heat  
83 fluxes, reporting a net heat budget of  $2 \pm 12 \text{ W m}^{-2}$  and noting a warm bias in this ensemble estimate. Utilizing an  
84 ensemble of high-resolution regional climate models (RCMs), Sanchez-Gomez et al. (2011) found that individual  
85 RCMs did not achieve a heat budget closure, but the ensemble mean heat flux was  $-7 \pm 21 \text{ W m}^{-2}$ . Using downscaled  
86 NCEP/NCAR global reanalysis of  $\frac{1}{2}^\circ \times \frac{1}{2}^\circ$  resolution, Ruiz et al. (2008) computed a net heat budget of  $-1 \text{ W m}^{-2}$ .  
87 However, their heat flux components values are not close to most of the literature values (for instance, the major  
88 difference was in the value for net short wave with  $84 \text{ W m}^{-2}$ ). Marullo et al. (2021) recently analysed several  
89 atmospheric data sets, revealing a significant net heat flux variability ranging between  $1.6$  and  $40 \text{ W m}^{-2}$ . They  
90 attributed this variability primarily to longwave radiation fluxes uncertainties. In addition to these challenges, past  
91 studies of air-sea fluxes have primarily focused on establishing mean and variance, leaving limited knowledge about  
92 their statistical distributions (Korolev et al., 2015; Tian et al., 2017). Understanding the probability distributions of  
93 air-sea fluxes and their higher moments could provide insights into the uncertainties associated with air-sea physics.  
94 Also, the analysis of probability distributions can help to assess skills of different reanalyses to replicate extreme  
95 fluxes (Gulev and Belayaev, 2012).

96 In this study we investigate two different aspects of the surface heat budget closure hypothesis. First, we employ  
97 two different high quality surface atmospheric variable data sets at different horizontal resolution and we calculate  
98 the heat fluxes with the same bulk formula and the same SST. This isolates the impact of atmospheric model  
99 resolution and quality as the source of variation in the heat flux estimates. Therefore, we answer the question: is  
100 the Mediterranean Sea in the past 15 years still losing heat at the surface?

101 Secondly, we study the statistical distributions of the heat flux components, utilizing the atmospheric analysis dataset  
102 from ECMWF (European Centre for Medium-Range Weather Forecasts). Knowing the skewness and kurtosis  
103 distributions across the basin, we analyse the extremes of the net heat budget, and we determine the specific  
104 importance of the extreme heat losses to the long-term mean. The second question we address is: what is the cause  
105 of the Mediterranean Sea negative long-term mean heat budget?

106 The paper is structured into the following sections. Section 2 presents the atmospheric analysis and reanalysis  
107 datasets from ECMWF, along with satellite SST data and the bulk formula used in the estimation of the fluxes. In  
108 Section 3, we present the new values of the heat budget closure problem, compared to the literature. In section 4,  
109 we analyse the probability distributions of turbulent heat fluxes. In Section 5, we determine the causes of the long  
110 term mean net heat budget values. Finally, Section 6 summarizes the findings and highlights key insights gleaned  
111 from this research.

112

113

114

## 115 2. Methodology and datasets

### 116 2.1 Air-sea physics in the Mediterranean Sea

117 For the Mediterranean Sea, several formulations have been established over the past decades through extensive  
118 studies. In this section, we present these adopted formulations, beginning with the net heat flux formula, followed  
119 by the specific heat flux components utilized in this study.

120 The net surface heat flux,  $Q_{net}$  comprises the net shortwave radiation  $Q_{SW}$ , net longwave radiation  $Q_{LW}$ , and surface  
121 turbulent flux components, which encompass the latent heat flux of evaporation  $Q_{LH}$  and sensible heat flux  $Q_{SH}$   
122 (Cronin et al., 2019; Pettenuzzo et al., 2010).

$$123$$
$$124 \quad Q_{net} = Q_{SW} + Q_{LW} + Q_{lat} + Q_{sen} \quad (1)$$
$$125$$

126 Here, we use the convention that positive heat fluxes denote heat gain by the ocean. We did not use directly the  
127 atmospheric model heat flux values since we wanted to intercompare two different atmospheric data sets in terms  
128 of their quality and resolution not on the basis of the specific bulk parametrizations and SST used. Thus, we used  
129 the same bulk formula and SST for both ECMWF and ERA5 surface variables that are described in section 2.2.

130

#### 131 2.1.1 Shortwave radiation flux

132 The shortwave radiation flux (SW) is derived from the formulation proposed by Rosati and Miyakoda (1988). The  
133 largest heat flux component is the solar radiation which is reduced by the cloud coverage and partially reflected by  
134 the sea surface (albedo). The shortwave heat flux formula is therefore expressed as:

$$135$$
$$136 \quad Q_{SW} = Q_{TOT} (1 - 0.62 C + 0.0019 \beta)(1 - \alpha) \quad \text{if } C \geq 0.3 \quad (2)$$

$$137 \quad Q_{SW} = Q_{TOT} (1 - \alpha) \quad \text{if } C < 0.3$$

138 where  $Q_{TOT}$  indicates the clear sky solar radiation calculated with astronomical formulae,  $\beta$  is the noon solar altitude  
139 in degrees and  $\alpha$  is the ocean surface albedo varying month wise values taken from Payne (1972). For the cloud  
140 cover, we follow the Reed (1977) formula, where the threshold cloud fraction 0.3 is in tenths, indicating 30% cloud  
141 coverage. The incoming solar radiation varies on locations with sun zenith angel and  $Q_{TOT}$  reaches at the ocean  
142 surface after diffusion can be represented by the components: the sum of the direct solar radiation  $Q_{DIR}$  for direct  
143 solar radiation and  $Q_{DIF}$  for downward diffused radiation. Then net solar radiation  $Q_{TOT}$  can be represented by the  
144 summation of components  $Q_{DIR}$  and  $Q_{DIF}$  :

$$145$$
$$146 \quad Q_{TOT} = Q_{DIR} + Q_{DIF}$$
$$147 \quad = Q_0 \tau^{\sec z} + [(1 - A_a) Q_0 - Q_0 \tau^{\sec z}] * 0.5$$

148 Here  $Q_0$  is the solar radiation at the top of atmosphere,  $\tau$  is equal to 0.7 and is the atmospheric transmission  
 149 coefficient,  $A_a$  is a constant value (0.09) and  $z$  is the sun zenith angle.

150

### 151 2.1.2 Longwave radiation flux

152 The longwave surface radiation **flux is** the difference between the upward infrared radiation (IR) emitted from the  
 153 ocean surface (LU) and the atmospheric downwelling infrared radiation (LD). The LD component is adapted from  
 154 Bignami et al. (1995), and the longwave radiation flux is written as:

155

$$156 \quad Q_{LW} = Q_{LU} + Q_{LD} \quad (3)$$

$$157 \quad Q_{LU} = -\epsilon \sigma_{SB} T_S^4 \quad (4)$$

$$158 \quad Q_{LD} = [\sigma_{SB} T_A^4 (0.653 + 0.00535 e_A)](1 + 0.1762 C^2) \quad (5)$$

159

160 where:  $T_S$  and  $T_A$  indicate the sea surface temperature and air temperature in degrees Kelvin,  $\sigma_{SB}$  is the Stefan-  
 161 Boltzmann constant,  $\epsilon$  is the ocean emissivity set to 1 according to Large and Yager (2009) and  $e_A$  is the atmospheric  
 162 vapor pressure computed from the mixing ratio of the air  $W_{air}$  (Wallace and Hobbs, 2006).

$$163 \quad W_{air} = \frac{q_A}{1 - q_A} \quad (6)$$

$$164 \quad e_A = \frac{W_{air}}{(W_{air} + \gamma)} p \quad (7)$$

165 and  $q_A$  is the specific humidity of air,  $p$  is the surface air pressure, and  $\gamma$  is a constant (0.622).

166 The specific humidity ( $q_A$ ) saturated at the  $T_A$  is computed using the following equation (Large, 2006), where  $\rho =$   
 167  $1.22 \text{ kg m}^{-3}$  is the air density:

$$168 \quad q_A = \rho^{-1} 640,380 \exp(-5107.4/T_D) \quad (8)$$

169 where,  $T_D$  is the dew point temperature retrieved from the atmospheric model outputs.

170

### 171 2.1.3 Turbulent heat fluxes

172 The turbulent heat flux is composed of sensible heat  $Q_{SH}$  and latent heat  $Q_{LH}$  given by the following formula:

$$173 \quad Q_{SH} = -\rho_A C_P C_H |\vec{V}| (T_S - T_A) \quad (09)$$

$$174 \quad Q_{LH} = -\rho_A L_E C_E |\vec{V}| (q_S - q_A) \quad (10)$$

175

176 where  $|\vec{V}|$  is the wind speed,  $\rho_A$  is the density of moist air,  $C_p$  is the specific heat capacity ( $1005 \text{ J g}^{-1}\cdot\text{K}$ ),  $C_H$  and  
177  $C_E$  are turbulent exchange coefficients for temperature and humidity,  $L_E$  is the latent heat of vaporization,  $q_A$  is  
178 defined in (8) and  $q_S$ , which is the specific humidity of air saturated at the sea surface temperature  $T_S$ , is calculated  
179 with (8) using  $T_S$  instead of  $T_D$ , and applying a 0.98 factor (Sverdrup, 1942). Since the average wind speed in the  
180 Mediterranean is 5 m/s, Pettenuzzo et al. (2010) suggested using constant turbulent exchange coefficients such as  
181  $C_H = 1.3 \cdot 10^{-3}$  and  $C_E = 1.5 \cdot 10^{-3}$ .

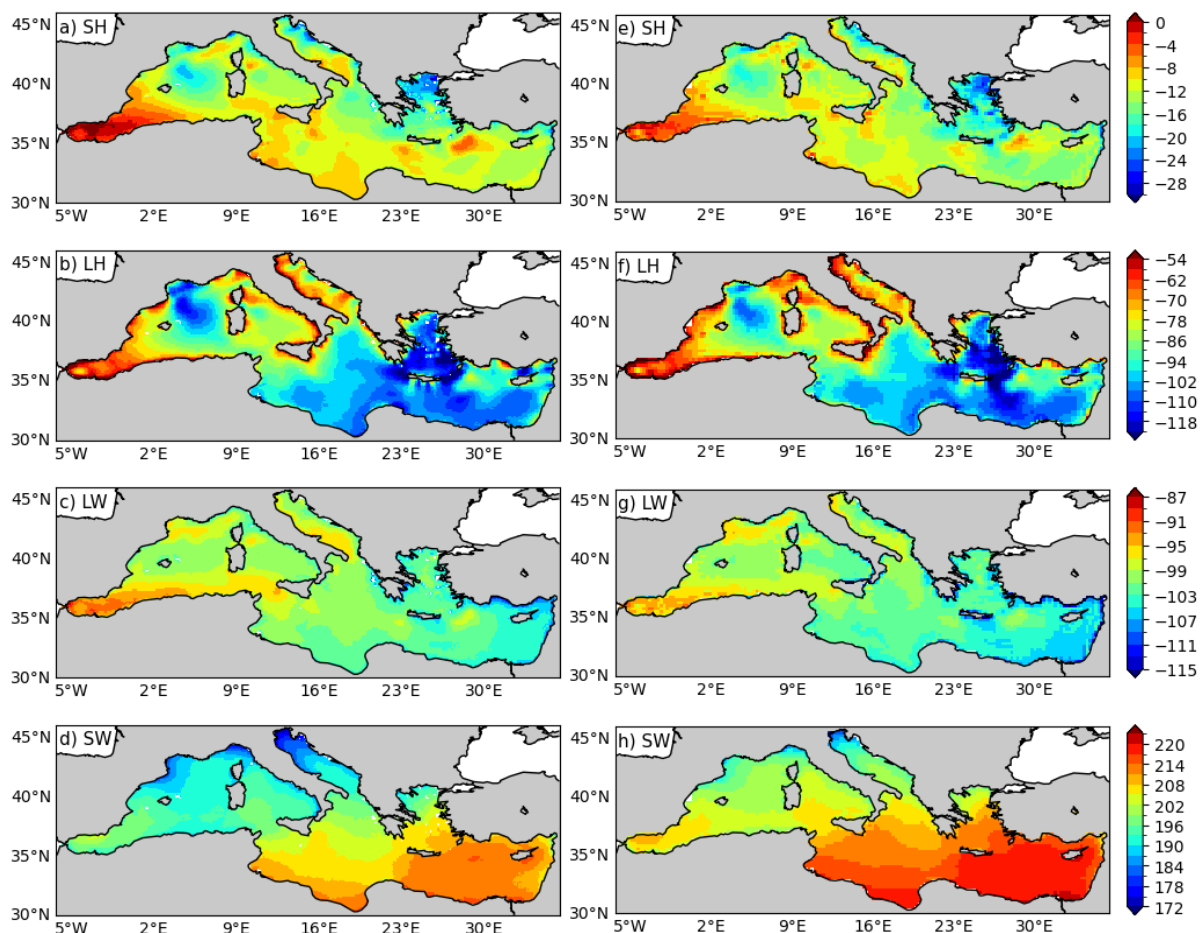
182

## 183 **2.2 Datasets**

184 Two atmospheric datasets have been selected for this study. The first dataset is the ECMWF (European Centre for  
185 Medium-Range Weather Forecasts) high-resolution analysis dataset (Rabier et al., 2000) at six-hourly temporal  
186 resolution and 0.125 degrees of spatial resolution. It's worth noting that the original operational dataset, from which  
187 the atmospheric fields have been extracted, underwent changes between 1991 and 2006 in terms of model resolution  
188 and the assimilated number of observations. For consistency, we opted to utilize the dataset with approximately  
189 uniform model resolution and physics spanning a 15-year period from 2006 to 2020. The second dataset employed  
190 is ERA5 reanalysis (Hersbach et al., 2020). This dataset is available at hourly intervals. However, it features a  
191 horizontal resolution of 0.25 degrees.

192 To mitigate unresolved atmospheric temperature daily cycles in ECMWF and make the two data sets consistent for  
193 the time variability, the ECMWF and ERA5 fields are further processed into daily mean values for the entire period.  
194 Comparisons conducted with daily and six-hourly input fields indicated minimal differences in the probability  
195 distributions of the heat fluxes, leading us to prioritize filtering out daily variability to the greatest extent possible.

196 To compute the heat fluxes the following atmospheric surface variables are extracted from the two datasets: the 10-  
197 meter wind components (U for the zonal direction and V for the meridional direction), mean sea level pressure, dew  
198 point temperature, total cloud coverage, and 2-meter air temperature.



199  
 200 **Figure 1: Annual means of** heat flux components for the period of 2006-2020, computed from ECMWF (left  
 201 panel) and ERA5 (right panel) daily time series. The corresponding ECMWF time series is shown in  
 202 supplementary material, Fig. S1 and S2.

203  
 204 For the oceanic SST data, we utilized the satellite dataset distributed by the Copernicus Marine Environment Service  
 205 (CMEMS). This SST dataset is a blended product from multiple satellite sensors, categorized as L4, with a  
 206 horizontal resolution of  $0.05^\circ \times 0.05^\circ$ . To align the SST data with the atmospheric analysis and reanalysis dataset  
 207 grids, we applied an interpolation and extrapolation method known as the 'sea-over land' (De Dominicis et al., 2013).  
 208 This method involves an iterative process to extrapolate sea values over land before interpolating, thus not allowing  
 209 the contamination of land values on the interpolation.

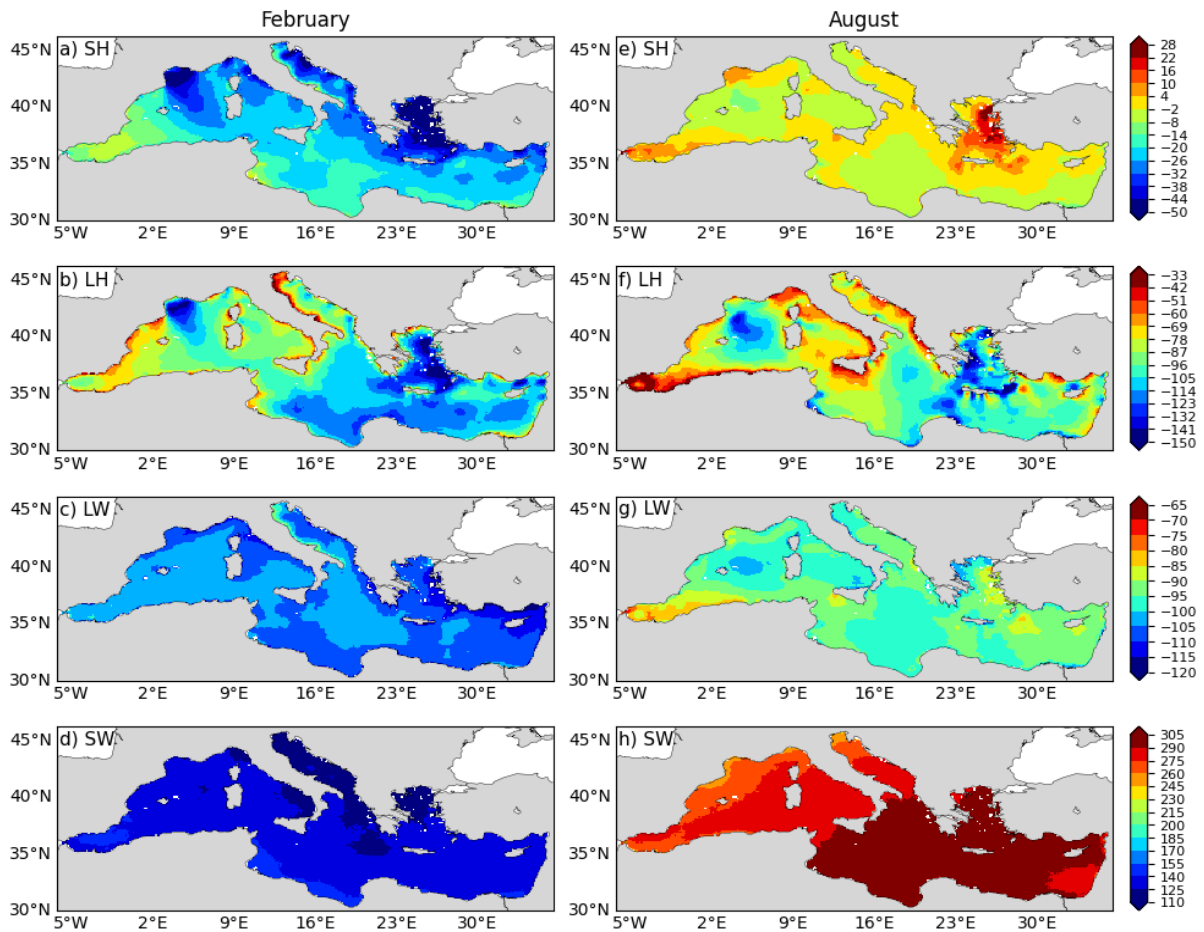
210  
 211 **3. Heat budget closure problem revisited**

212 **3.1 Analysis of the heat budget components**

213  
 214 We compute the heat fluxes for the 15-year period, 2006–2020, using the ERA5 dataset and compare them with the  
 215 fluxes computed using the ECMWF dataset (Fig. 1). In Fig. 1 we show the results for the 15-year mean of each  
 216 heat budget components. We start describing the ECMWF patterns and then we detail the differences.

217 Turbulent heat fluxes exhibit distinct sub-basin-scale patterns, varying between the eastern and western  
218 Mediterranean Seas as well as the Central Mediterranean region. The smallest mean sensible heat loss is observed  
219 in the whole Alboran sea area with absolute value range of 0-6  $\text{W m}^{-2}$ , while the Aegean Sea and the centre of Gulf  
220 of Lion loses more heat in the maximum value of 25  $\text{W m}^{-2}$ . Similarly, the highest absolute values of LH are  
221 recorded in the Gulf of Lion and the Aegean and Levantine Seas, attributed to the influence of strong and cold winds  
222 like the Mistral and Etesian in the north-western and eastern Mediterranean regions, respectively. The eastern  
223 Mediterranean emerges as the region with the highest evaporation, reaching approximately 122  $\text{W m}^{-2}$  in absolute  
224 value. Notably, along the south-eastern coastline, a wide range of maximum absolute values (102-122  $\text{W m}^{-2}$ ) in  
225 the evaporation is observed. The turbulent heat fluxes show limited differences between the ECMWF and ERA5  
226 datasets.

227 SW fields show the well-known meridional gradients with larger gradient values arising from the ECMWF dataset.  
228 The mean SW exhibits a gradual decline from the eastern to western Mediterranean, influenced by the variation of  
229 the solar zenith angle with longitudes. The first reason for SW differences between Western Mediterranean and  
230 Eastern Mediterranean is the latitudinal position of each sub-basin. Furthermore, SW differences using ECMWF  
231 and ERA5 datasets are connected to different cloud cover schemes (not shown), leading to a larger heat gain in the  
232 Eastern Mediterranean. Notably, the northern Adriatic region stands out with a distinct distribution, suggesting it  
233 receives relatively less annual solar radiation compared to other areas. In contrast, the mean longwave (LW)  
234 radiation distribution maintains a relatively consistent range of absolute values between 87–113  $\text{W m}^{-2}$  across the  
235 entire domain with absolute minimum values in the Alboran Sea, presumably due to the warm Atlantic surface water  
236 inflow. Overall, while the turbulent heat fluxes show limited differences between the ECMWF and ERA5 datasets,  
237 significant discrepancies are observed in radiative heat fluxes. Additionally, Fig. 1 shows the noisiness of the fluxes  
238 due to the ERA5 low resolution with respect to ECMWF while retaining an overall consistency.



239  
 240 **Figure 2: Seasonal variations of heat flux components: Left column is the monthly average values for**  
 241 **February and right column shows the average for August for the period 2006-2020 (ECMWF data).**

242  
 243 Figure 2 shows seasonal variations in heat flux components for February and August using ECMWF data. Both SH  
 244 and LH fluxes exhibit a greater spatial gradient in February compared to August. In winter, the SH loss is larger,  
 245 especially in the Gulf of Lion, Aegean, and parts of the Adriatic, with stronger spatial gradients compared to summer.  
 246 In August, SH flux becomes positive in the Aegean and the Alboran Sea. LH loss is highest in February in the whole  
 247 eastern Mediterranean and the Gulf of Lion. In August, LH losses decrease in the western Mediterranean, with  
 248 absolute value minima in the Alboran and Adriatic Sea, remaining largely negative in the lower part of in the Eastern  
 249 Mediterranean. SW fields show the strongest seasonal cycle as expected, with the absolute maximum of 260-305  
 250  $W m^{-2}$  in summer and in the Eastern Mediterranean. LW is largest in absolute value in winter showing a small  
 251 seasonal cycle. Significant seasonal variations are observed in the distribution range for radiative heat fluxes, low  
 252 in February and high in August across the entire domain. These patterns are quite similar to the ones reported in the  
 253 literature.

254  
 255  
 256

### 257 3.2 Net heat budget estimation

258

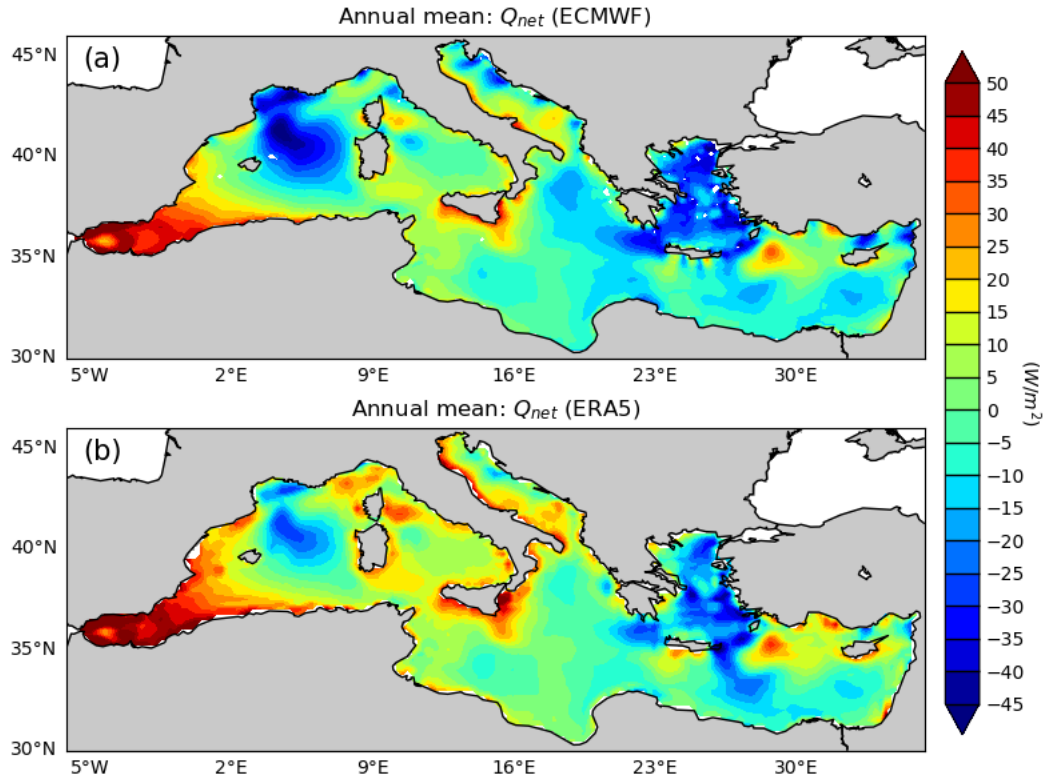
259 The net surface heat flux  $Q_{net}$  is depicted in Figure 3 for ERA5 and ECMWF and basin-average 15 year mean  
260 values are listed together with the literature in Table 1.

261 Fig. 3 shows that the Gulf of Lion and the Aegean Sea are the areas of maximum heat losses while the basin gains  
262 heat in the Alboran Sea, in some areas of the Levantine basin, and in the shelf areas around the Italian peninsula.

263 The Mediterranean Sea gains comparatively more heat with the ERA5 inputs. Besides the difference in surface  
264 domain for  $Q_{net}$ , for both cases, air-sea flux dynamics is strongly visible in the Alboran Sea for net heat gain, in  
265 the Gulf of Lion for heat loss due to the continental cold wind (Mistral wind), and in the Aegean Sea due to the  
266 strong wind (Etesian wind) that blows during the summer period. Using ECMWF inputs,  $Q_{net}$  is  $-3.6 \text{ W m}^{-2}$ , a value  
267 consistent with previous estimates for the Mediterranean Sea domain and for ERA5, it is  $5 \text{ W m}^{-2}$  (Table 1). Errors  
268 in  $Q_{net}$  mean value are determined by a bootstrapping method where  $Q_{net}$  time series is resampled 5000 times to  
269 compute a standard deviation around the mean of the resampled time series (Tibshirani & Efron, 1993). We argue  
270 that our results show that the negative heat budget is achieved by using only ECMWF fields at high resolution, i.e.  
271  $0.125$  degrees. Higher resolution implies differences in all atmospheric fields used to compute the fluxes.  
272 Furthermore, ERA5 and ECMWF model physics and dynamics is different contributing to the differences in the  
273 mean heat budget. However, both datasets use observations, and we argue that the most relevant difference between  
274 the analysis and the reanalysis data set is the resolution due to the peculiar geometry of the Mediterranean Sea.

275 Since all the datasets [used in the literature](#) are coarser, this is most likely the reason of the failure to determine the  
276 correct heat budget closure value. In Pettenuzzo et al. (2010) several ad-hoc corrections were made to the surface  
277 atmospheric fields to obtain the negative heat flux budget while in Sanchez-Gomes et al., (2011) they used an  
278 ensemble of deterministically downscaled ERA40 fluxes giving rise to a very large uncertainty. Considering a  
279 recent literature, our resulted  $Q_{net}$  is closely matched with the computed net heat budget of  $-3 \pm 8 \text{ W m}^{-2}$  from Jordà  
280 et al., (2017), but their result was associated to large temporal uncertainties from the surface fluxes through Gibraltar  
281 Strait.

282



283

284 **Figure 3: Comparison of the annual  $Q_{net}$  ( $W m^{-2}$ ) mean, computed from a) ECMWF and b) ERA-5 input**  
 285 **datasets.**

286 **Table 1: Computed heat flux components and net heat fluxes ( $Q_{net}$ ), and values from the references**

Authors	SH	LH	LW	SW	Net Flux ( $Q_{net}$ )
Bethoux (1979)	-13	-120	-68	195	-6
Bunker (1982-1)	-13	-101	-68	202	20
Bunker et al (1982-2)	-11	-130	-68	202	20
May (1986)	-11	-130	-68	193	2
Garret et al. (1993)	-7	-99	-67	202	29
Matsoukas et al. (2005)	-11	-122	186	-63	22
Ruiz et al. (2008)	-8	-88	-73	168	-1
Pettenuzzo et al. (2010)	-14	-90	-79	178	-7
Sanchez-Gomez et al. (2011)	-13±5	-100±13	-75±6	181±18	-7±21
Criado-Aldeanueva et al. (2012)	-15.1	-93.5	-76.9	186.3	0.73
Song & Yoy (2017)	-13±4	-98±10	-78±13	192±19	2±12
Jordá, et al., 2017	-	-	-	-	-3±8
ECMWF analyses	-12.1±4	-92±16	-100.5±3	201±8	-3.6±1.3
ERA5 reanalysis	-13±3	-89±14	-101±3	208±8	5±1.2

287 Spatially, the mean  $Q_{net}$  distribution generally shows a heat loss across much of the Eastern Mediterranean. Overall,  
 288 distributions of more positive net heat budget values for the western Mediterranean and negative for the eastern  
 289 Mediterranean have matched with the similar result from Criado-Aldeanueva et al. (2012). Strong spatial gradients  
 290 are evident, particularly in the Aegean Sea, although a few patches displaying net heat loss (negative  $Q_{net}$ ) are also  
 291 noticeable in this vicinity. Conversely, the western Mediterranean exhibits a stronger heat gain area, which appears  
 292 particularly concentrated zone in the Gulf of Lion region and this feature is apparent in results from both atmospheric  
 293 datasets. Such a spatial related uncertainty in  $Q_{net}$  represents a significant challenge for accurately closing regional  
 294 heat budgets as well as validating existing ocean circulation models within the complex Mediterranean basin.

295

#### 296 **4. Probability distributions of the turbulent heat fluxes**

297 In this section, we analyse the probability distribution of turbulent heat fluxes computed using ECMWF data set  
 298 only and for the anomaly heat fluxes. Recent studies by Gulev and Belyaev (2012) and Korolev et al. (2015) have  
 299 analysed the statistical distributions of turbulent heat fluxes, and their findings are used here for comparison.  
 300 Radiative flux components are excluded from this analysis, as they do not exhibit extremes of comparable magnitude  
 301 to those of turbulent fluxes (Supplementary material, Fig S3). This suggests low skewness and kurtosis in their  
 302 distributions, reducing the relevance of a detailed probability density function analysis for these components.

303

304 If we indicate the time series of each component of the heat budget with  $X_n$  we can define the heat flux climatology  
 305 as:

306

$$307 \quad Q_t = \frac{1}{n} \sum_{j=1}^n X_{tj} \quad (11)$$

308

309 where ‘t’ indicates the day of the year, and ‘j’ is the number of years. The anomaly time series is computed by  
 310 subtracting the long-term seasonal climatology  $Q_t$  from the observed heat flux time series  $X_{tj}$  and it will be indicated  
 311 by:

312

$$313 \quad \tilde{X}_{tj} = X_{tj} - Q_t \quad (12)$$

314

#### 315 **4.1 SH flux distribution**

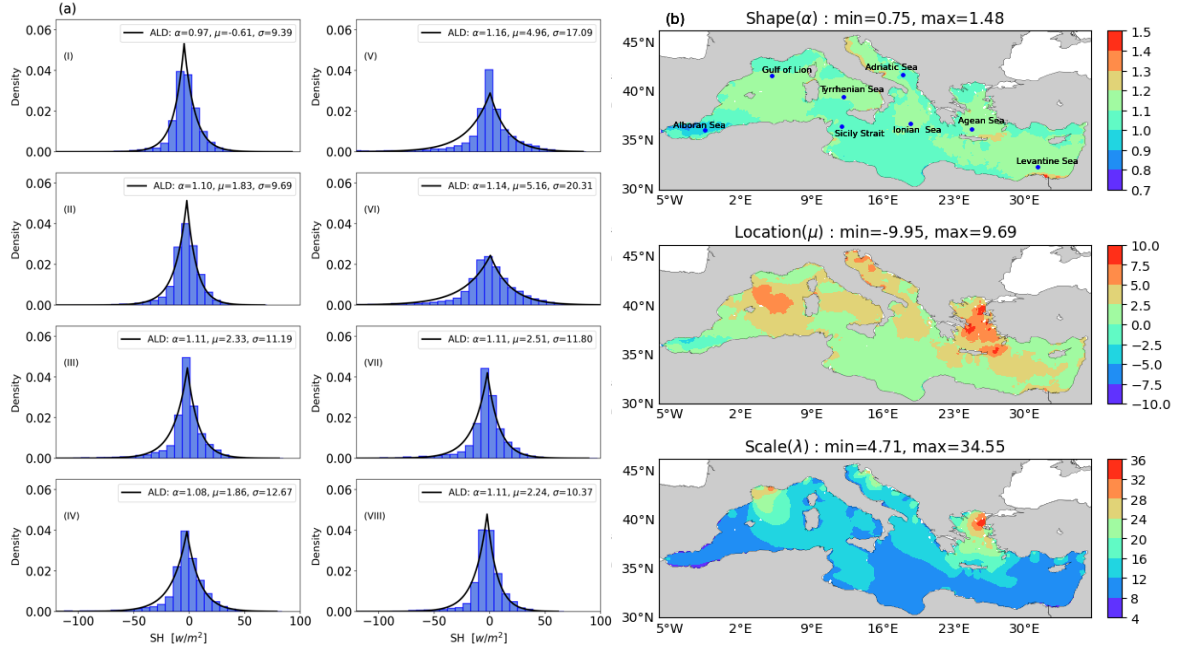
316 We found that gaussian or skew-normal distributions are not well fit for SH flux, as evident from the histograms at  
 317 single grid points shown in Figure 4a. The histograms reveal a singularity around zero, indicating that the skew-  
 318 normal distribution may not adequately capture the distribution of these values. This observation is consistent with  
 319 findings by Gulev and Belyaev (2012), and we provide further explanation in the Appendix A.

320 The most common distribution with such near-discontinuous behaviour at the origin is the three-parameter  
 321 Asymmetric Laplace Distribution (ALD) (Yu & Zhang, 2005) that we can defined as

322 
$$F(x, \alpha, \mu, \lambda) = \frac{\lambda}{\alpha + \frac{1}{\alpha}} \begin{cases} \exp\left(\frac{\lambda}{\alpha}(x - \mu)\right) & \text{if } x < \mu \\ \exp(-\lambda \alpha(x - \mu)) & \text{if } x \geq \mu \end{cases} \quad (13)$$

323 where  $x$  is the random variable time series,  $\alpha$  is the shape parameter,  $\mu$  is the location and  $\lambda$  the scale.

324



325  
 326 **Figure 4: a) The single grid point histograms for SH flux anomalies from the eight sampling locations for the**  
 327 **period of 2006–2020, 4 b) The Asymmetric Laplace PDF parameter ( $\alpha$ ,  $\mu$ ,  $\lambda$ ) distributions from computed SH**  
 328 **flux anomaly for the observation period. [Sampling points: (I) Alboran Sea, (II) Gulf of Lion, (III) Tyrrhenian**  
 329 **Sea, (IV) Sicily Strait, (V) Adriatic Sea, (VI) Ionian Sea, (VII) Aegean Sea, (VIII) Levantine Sea]**

330  
 331 From the single grid point histogram, we have observed a one or two sharp peaks in the distribution that matches  
 332 well with the Asymmetric Laplace Distribution (ALD) PDF. In accordance with findings by Yu and Zhang (2005),  
 333 the distribution of the sensible heat (SH) flux anomaly time series exhibits characteristics of a double exponential  
 334 distribution. This is evident from the histograms displaying both positive and negative skewness with long tails, as  
 335 depicted in Figure 4a. The ALD parameters for the SH flux anomaly time series are illustrated in Figure 4b. The  
 336 shape parameter ( $\alpha$ ) falls within the positive range of 0.73 to 1.48, indicating a moderate to high degree of peakiness  
 337 in the distribution. Additionally, the location parameter ( $\mu$ ) exhibits mostly positive values while a small area in the  
 338 Alboran Sea shows negative values, suggesting a shift in the central tendency of the distribution. Notably, the scale  
 339 parameter ( $\lambda$ ) displays a similar structure to the SH flux climatology depicted in Figure 1.

340 To check the quality of the fit, moments of both applied and theoretical PDF are compared (presented in  
 341 supplementary materials, Fig. S4). The comparison shows the estimations of the three moments in the left panel for  
 342 the observed SH flux and right panel for ALD PDF parameters. It can be seen that variances and skewness are  
 343 similar in distribution while kurtosis differ at noticeable range. This observation is likely attributed to the fact that  
 344 the kurtosis for the asymmetric Laplace distribution remains constant regardless of changes in the scale parameter.

345

## 346 4.2 LH flux distribution

347 In the case of the LH flux, no sharp exponential peaks were observed; instead, large skewness and long tails were  
348 identified. Therefore, we applied the skew-normal PDF which is defined by  $\alpha$  ( $\in \mathbb{R}$ ) as the shape parameter,  $\mu$  ( $\in$   
349  $\mathbb{R}$ ) the location parameter, and  $\lambda > 0$  the scale parameter (Azzalini, 1985) and defined as:

$$350 \quad f(x, \alpha, \mu, \lambda) = \frac{2}{\lambda} \phi\left(\frac{x-\mu}{\lambda}\right) \Phi\left(\alpha \frac{x-\mu}{\lambda}\right) \quad (14)$$

351

352 Where,

$$353 \quad \phi\left(\frac{x-\mu}{\lambda}\right) = \frac{1}{\sqrt{2\pi}} e^{-\frac{1}{2} \frac{(x-\mu)^2}{\lambda^2}} \quad (15)$$

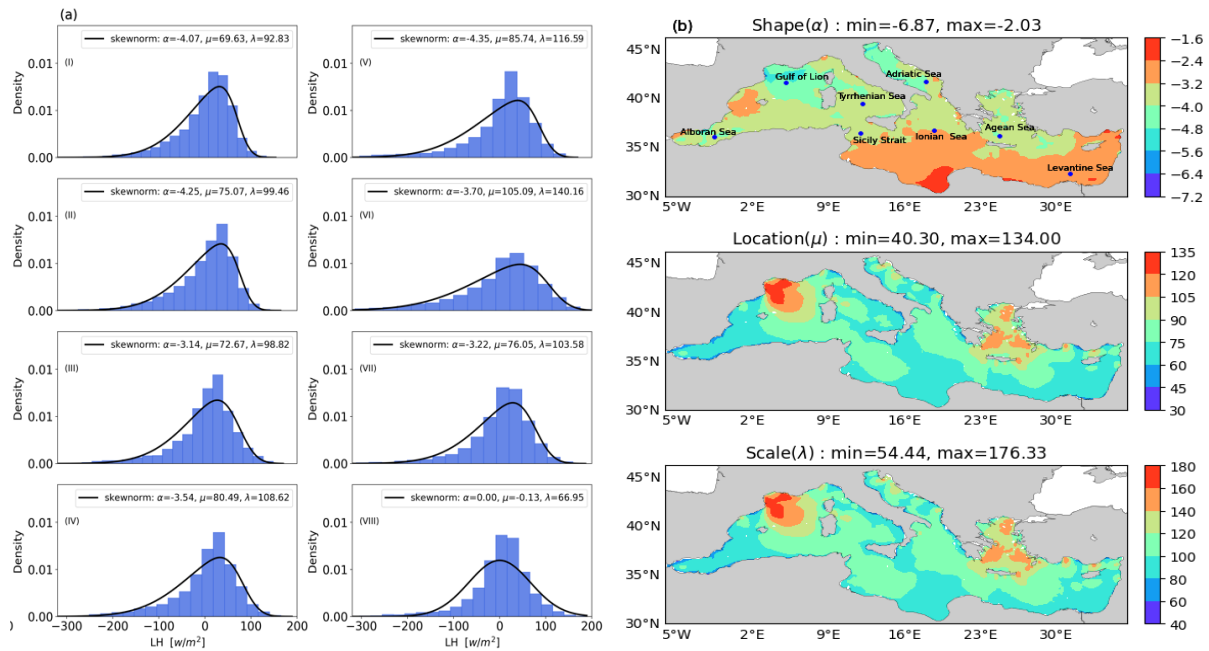
$$354 \quad \Phi\left(\alpha \frac{x-\mu}{\lambda}\right) = \int_{-\infty}^{\alpha \frac{x-\mu}{\lambda}} \phi(t) dt \quad (16)$$

355

356 A skew-normal PDF is an extension of the normal distribution while covering the skewness and containing the  
357 general characteristics of a Gaussian distribution (Flecher et al., 2010).

358 To examine visually the quality of PDF fit on LH flux anomaly values, histograms from eight sea locations were  
359 fitted with the skew-normal PDF, as shown in Figure 5a. Figure 5b displays the parameter spatial variability. The  
360 shape parameter distribution ranges from -6.83 to -2.5, with negative values observed across all points. This spatial  
361 distribution of  $\alpha$ , exhibiting a negative range, aligns with the negatively skewed pattern identified in the single grid  
362 point PDF fitting test. Furthermore, the spatial distribution structure of the location and scale parameters  
363 demonstrates a positive correlation across most locations.

364 In the Supplementary material, a comparison of statistical moments is conducted to qualitatively validate the fit  
365 (supplementary materials, Fig S5). There is notable agreement in the variance distributions between the observed  
366 LH flux anomaly and skew-normal PDF. While the skewness distributions mismatch at negligible level, with the  
367 theoretical PDF skewness predominantly ranging from -0.9 to -0.3, whereas the observed skewness exhibits a  
368 variation range spanning from -1.2 to over -0.3. Lastly, the kurtosis distribution of the skew-normal PDF differs in  
369 the Aegean Sea, Alboran Sea and Gulf of Lion area.



371 **Figure 5: a) The single grid point histograms for LH flux anomalies at the eight sampling locations for the**  
 372 **period of 2006-2020, 5 b) The skew-normal PDF parameter ( $\alpha$ ,  $\mu$ ,  $\lambda$ ) distributions for computed LH Flux**  
 373 **anomaly for the observation period [Sampling points: (I) Alboran Sea, (II) Gulf of Lion, (III) Tyrrhenian**  
 374 **Sea, (IV) Sicily Strait, (V) Adriatic Sea, (VI) Ionian Sea, (VII) Aegean Sea, (VIII) Levantine Sea]**

375

### 376 4.3 Evaluation of the PDF fitting

377 In this section, we conducted a goodness of fit test to measure the distance between the empirical distributions and  
 378 the fitted ones. The objective of this evaluation test was to assess the degree of agreement between the applied  
 379 theoretical distribution and the observed time series. The chi-squared method, a well-accepted test, was employed  
 380 to measure the distance between two independent distributions.

381 We compared the results of the chi-squared test for the turbulent heat fluxes computed using the ECMWF and ERA5  
 382 datasets. The decision rule for the  $\chi^2$  test was determined based on the level of significance, set at 0.05, and the  
 383 degrees of freedom, defined as  $DF = N - np$ , where  $N$  represents the number of empirical histogram bins and  $np$   
 384 is the number of distribution parameters (i.e., 3 for both the ALD and skew-normal distributions). In the  
 385 supplementary material we show the maps of Chi-square test statistics (Supplementary material, Fig. S6). The chi-  
 386 squared results for the SH and LH fluxes computed using the ECMWF dataset indicate that almost all surface grid  
 387 points are well-fitted with the applied theoretical PDFs. With the critical threshold of 33.92 (Elderton, 1902) for  $P$   
 388 values, we observed a very few mismatches, mainly located near the coasts.

389

## 390 5. How do heat loss extremes contribute to the heat budget closure hypothesis?

391 The heat budget closure problem is associated with achieving a net negative heat flux, as discussed before. We test  
 392 here the hypothesis that the negative long term mean negative heat budget of Table 1 for ECMWF data is correlated  
 393 to the extremes in heat losses during autumn-winter.

394 Figure 6 illustrates the  $Q_{net}$  basin average daily time series, revealing a value range varying between 200 and -500  
 395  $W m^{-2}$ . Notably, the most pronounced extreme negative heat losses, reaching up to  $-500 W m^{-2}$  occur in the winters  
 396 of 2011, 2015 and 2017. They approximately coincide with western Mediterranean Deep Water formation events,  
 397 as documented in Escoudier et al. (2021). To identify and remove the potential extremes in our computed  $Q_{net}$  time  
 398 series, we apply the Interquartile Range (IQR) method which measures the spread of a dataset and calculate the  
 399 difference between the third quartile(Q3) and the first quartile (Q1). The IQR threshold is computed by the  
 400 difference between the 1<sup>st</sup> quartile (Q1) and 3<sup>rd</sup> Quartile (Q3) of the observed dataset:

401

$$402 \quad IQR = Q3 - Q1 \quad (17)$$

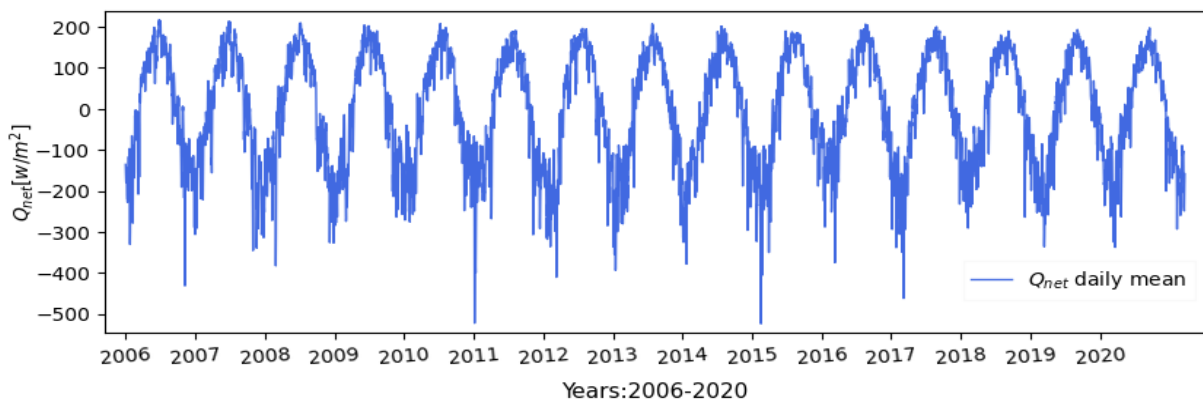
$$403 \quad \text{Threshold} = Q1 - k * IQR \quad (18)$$

404

405 We used different values for k to exclude the negative extremes, which correspond to the largest heat losses. These  
 406 extreme values were replaced with long-term daily climatological values (computed using eq. 11 and the long term  
 407 mean neat heat budget  $Q_{net}$  is recomputed.

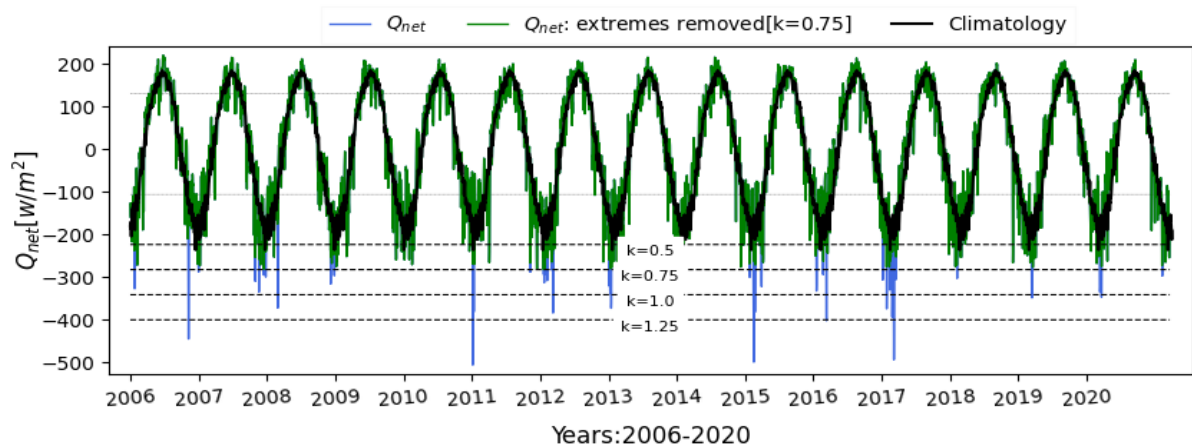
408 The resulting  $Q_{net}$  for different thresholds is displayed in Table 2 and the thresholds are shown in Fig. 7 together  
 409 with the daily climatology. If compared with the long term mean heat budget in Table 1 ( $-3.6 \pm 1.3 W m^{-2}$ ), we see  
 410 that eliminating the winter extremes produces a smaller long term mean heat loss up to changing the sign to positive  
 411 values. We argue that the ECMWF net negative heat extremes determine the ECMWF negative long term mean  
 412 heat budget. Furthermore, if we calculate the yearly mean value of the seasonal climatology, we obtain the value  
 413 of  $+4 W m^{-2}$ , which confirms again the importance of extremes in the heat budget closure of the Mediterranean  
 414 Sea.

415 The  $Q_{net}$  could become an impact indicator of the Mediterranean for sea level trends in the basin. The net heat  
 416 budget in fact relates to the sea level tendency (Pinardi et al., 2014) in the Mediterranean Sea and could be considered  
 417 as a key indicator of climate impacts in the Mediterranean Sea.



418

419 **Figure 6: Basin averaged time series of the computed daily  $Q_{net}$  (units  $W m^{-2}$ ) from the ECMWF computed**  
 420 **heat fluxes, for the period 2006-2020.**



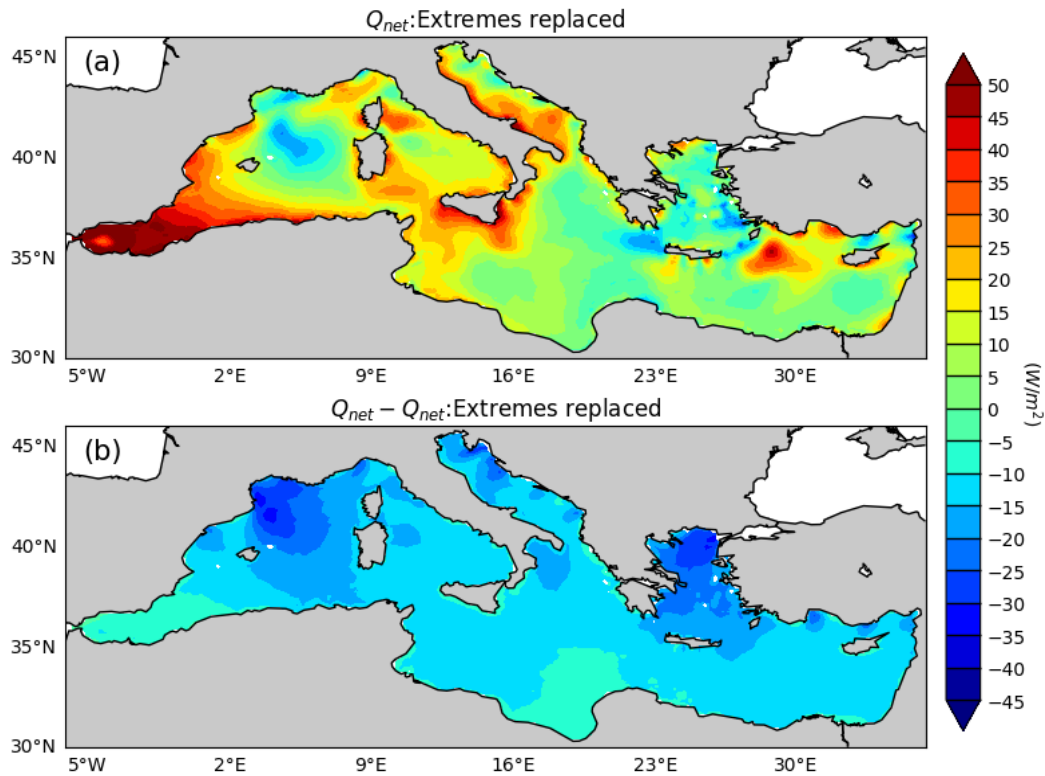
422  
 423 **Figure 7: Time series of the basin averaged  $Q_{net}$  mean,  $Q_{net}$  extremes removed mean, and long-term yearly**  
 424 **climatology and four lower quantile boundary line marked with dashed lines using different k values [k=1.25,**  
 425 **1,0.75, 0.5].**

426  
 427 **Table 2: Different lower quantile boundary limits used to replace potential extremes and the resulting long-**  
 428 **term mean basin averaged  $Q_{net}$  values**

IQR lower boundary limit	Threshold values ( $W m^{-2}$ )	$Q_{net}(W m^{-2})$
K=1.25	<u>-405</u>	-3.2
K=1.0	<u>-347</u>	-2.5
K=0.75	<u>-289</u>	-1
K=0.5	<u>-231</u>	2

429  
 430 Figure 8 presents the new long-term mean spatial distribution of the surface heat budget after removing negative  
 431 extreme values using a threshold of -289  $W m^{-2}$  (K = 0.75). The figure illustrates that these extreme events exert a  
 432 substantial influence on the overall structure of the net heat budget in the Mediterranean Sea, with particularly  
 433 pronounced effects in the Gulf of Lion, the Aegean Sea, the eastern Adriatic Sea, and along the southern Turkish  
 434 shelves.

435



436  
 437 **Figure 8: a) Long term mean net heat flux after the removal of extremes ( $Q_{net}$ :Extremes replaced) using**  
 438 **threshold of  $-289 \text{ W m}^{-2}$  ( $K = 0.75$ ) b) The time mean distribution computed from the difference between**  
 439  **$Q_{net}$  (Fig. 3a) and “ $Q_{net}$ : Extremes replaced” time series. It shows a significant reduction of heat losses in**  
 440 **the Gulf of Lion, Adriatic Sea and Aegean Sea regions.**  
 441

441

442

## 443 6. Discussion and conclusions

444

445 The primary objective of this investigation is to revisit the heat budget closure hypothesis from atmospheric  
 446 consolidated data sets that are nowadays used frequently to drive ocean models. Simultaneously, we intend to model  
 447 the statistical distributions of turbulent heat fluxes and assess the contribution of extremes into the net heat budget  
 448 closure of the Mediterranean Sea. For this analysis, we covered a 15-year period from 2006 to 2020 with a daily  
 449 time series frequency. The reason for the choice of this time range is that ECMWF analyses became quite stable  
 450 starting from 2006 while before the model was at coarse resolution, like ERA5’s model. Our strategy is to use the  
 451 same SST and the same bulk formula but different atmospheric reanalysis and analysis surface variable data sets  
 452 and compare the value of the long term mean heat budget in the Mediterranean Sea.

453 Firstly, the surface heat budget of the Mediterranean Sea was analysed to examine average annual mean and seasonal  
 454 variations. The largest component of the heat budget is the net solar radiation (SW), followed by the latent heat  
 455 (LH), longwave radiation (LW), and then sensible heat (SH), as shown in the literature (Table 1). All heat flux  
 456 components exhibit significant seasonality, as illustrated in Figure 2. Differences appear in the structure of the  
 457 fluxes, especially the SW and LW, when different atmospheric data sets are used, a conclusion aligning with a

458 suggestion from Marullo et al. (2021) on the sensitivity of LW estimates from the atmospheric dataset used to  
459 calculate fluxes. We compared the ERA5-derived surface radiative fluxes with [the computed ERA5 heat fluxes](#)  
460 [presented in Figure 3b](#) and found that the ERA5 longwave (LW) fluxes are substantially overestimated in absolute  
461 magnitude (Supplementary Material S7). The associated uncertainty is comparable in order of magnitude to that  
462 reported by Marullo et al. (2021), who analysed an observational dataset at a specific site. Nonetheless,  
463 compensating biases between the SW and LW components (Supplementary Material S8) result in a net radiative  
464 heat balance [difference between ERA5-derived and computed heat fluxes](#) that is large primarily in the southern  
465 Mediterranean, where ERA5-[derived](#) exhibits reduced LW flux values.

466  
467 The basin-average net heat flux,  $Q_{net}$ , was calculated to be  $-3.6 \pm 1.3 \text{ W m}^{-2}$  for ECMWF analysis data while it is  
468  $5 \pm 1.2 \text{ W m}^{-2}$  for ERA5 (Table 1). This finding supports the conclusion that heat budget closure hypothesis cannot  
469 be satisfied with a relatively coarse reanalysis atmospheric data set. Our initial question was: is the Mediterranean  
470 Sea in the past 15 years still losing heat at the surface? The answer is yes if we use a high-resolution ECMWF  
471 atmospheric analysis. Additionally, comparing the  $Q_{net}$  estimates derived from ERA5 and ECMWF with the same  
472 bulk formulas demonstrates that the uncertainty peaks in the atmospheric forcing resolution and possibly cloud  
473 cover, [the latter affecting the radiative components of the heat budget](#).

474  
475 Furthermore, we have demonstrated that the probability density of surface heat fluxes can be modelled and fitted  
476 with a three-parameter PDF composed of a shape, a location, and a scale parameter. All the turbulent heat flux  
477 components show asymmetric behaviour. There is encouraging agreement between the first two statistical moments  
478 of the fitted PDF and the observed values. Kurtosis does not seem to be properly captured by the PDF used but our  
479 time series is too short to arrive at a definitive conclusion. For the SH we demonstrate that the [Asymmetric Laplace](#)  
480 [Distribution](#) PDF is generated by the contributing distributions of wind speed (Weibull) and temperature difference  
481 [Skew Normal](#)). We believe this is the first time that such kind of [relationship](#) is demonstrated.

482 Gulev and Belyaev (2012) applied the two-parameter Fisher–Tippett distribution (also known as the Gumbel  
483 distribution) to monthly sensible and latent heat fluxes derived from NCEP–NCAR reanalysis fields. Their  
484 approach focused on using the mean and standard deviation to estimate the distribution’s location and scale  
485 parameters relevant to extreme events. However, the Gumbel distribution has a fixed skewness, limiting its ability  
486 to capture the contribution of rare, asymmetric extremes. In contrast, our study analysis anomalies from the seasonal  
487 cycle using full probability distributions that allow for variable skewness. This better reflects the nature of  
488 atmospheric and oceanic variables, which are often inherently skewed (Sardeshmukh and Penland, 2015), and is  
489 essential for understanding the influence of extremes on the surface heat budget. Our findings show that  
490 incorporating a shape parameter is key to accurately capturing distribution structure and preserving asymmetric  
491 tails. This analysis provides a useful framework for validating surface flux products and assessing their variability,  
492 particularly important given that surface fluxes are the dominant source of uncertainty in the Mediterranean net heat  
493 balance (Jordà et al., 2017). Correctly estimating skewness is crucial, as a small number of extreme outliers,  
494 especially during intense winter events, can disproportionately affect the basin-wide mean and determine whether  
495 heat budget closure is achieved.

496 For the first time, we have investigated the effects of extreme heat losses in the Mediterranean Sea in the long term  
497 mean basin averaged heat budget. The northern basin areas are the site of the largest heat losses (Gulf of Lion and  
498 the Aegean Sea, Adriatic Sea and the Turkish southern coasts). Exclusion of the negative extremes in these areas  
499 resulted in a change in the sign of long term mean heat loss. The anomaly threshold value ( $-231 \text{ W m}^{-2}$ , Table 2)  
500 resulted a long-term positive net heat flux, which is inconsistent with the basin's heat flux closure hypothesis. Our  
501 second initial question was: what is the cause of the Mediterranean Sea negative long-term mean heat budget? The  
502 answer is that the long-term mean, basin averaged heat loss is due to winter extremes in the Northern regions of the  
503 Mediterranean Sea.

504 In conclusion, understanding the characteristics and distributions of air-sea heat fluxes are crucial for gaining  
505 insights into variations in the heat budget. Furthermore, the PDF analysis of turbulent heat fluxes will allow us to  
506 have a better understanding of the extreme events and their contributions to the net negative heat budget. The next  
507 steps could involve a machine learning study of air-sea flux bulk parametrizations for different atmospheric data  
508 sets and coupled models, using as target the heat flux data set from this study.

509

510

511

512

513

514

515

516 **Data availability**

517  
518 The ERA5 data available at Copernicus Climate Change Service, Climate Data Store, (2023): ERA5 hourly data  
519 on single levels from 1940 to present. [https://cds.climate.copernicus.eu/datasets/reanalysis-era5-single-](https://cds.climate.copernicus.eu/datasets/reanalysis-era5-single-levels?tab=download)  
520 levels?tab=download . ECMWF analysis data can be arranged following the submission of a request.

521

522 **Author contributions**

523  
524 MHG: development of the concept, literature review, writing, methodology, coding, formal analysis, wiring,  
525 visualization. NP: conceptualization, review, writing, methodology. AN: conceptualization, writing, review. LM:  
526 review, writing. SB: methodology, review. FM: methodology, review. FT: methodology, coding.

527

528 **Acknowledgments**

529 This research has been funded from the University of Bologna under the Future Earth, Climate Change and Societal  
530 Challenges PhD Program for MHG. Additionally, there was a partial support from the Edito-Lab HEU project for  
531 MHG and NP.

532

533 **Conflict of interest Statement**

534 The authors declare no conflicting interests.

535

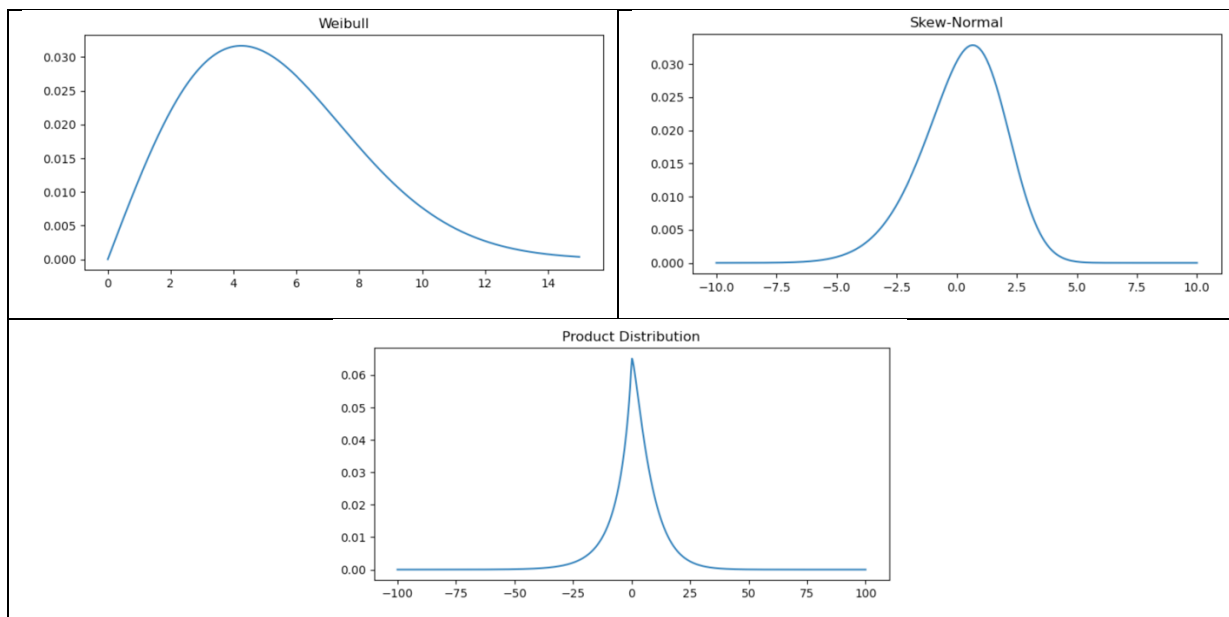
## APPENDIX A

536

537 Here, we show that the characteristics of the SH flux distribution are due to the specific form of the heat flux as  
538 given by (10), i.e. a multiplication of two distributions, wind speed, Q(v), known to be a Weibull, and temperature  
539 differences, R(DT), taken to be a Skew Normal.

540 Let's indicate with  $P(v*DT)$  the combined SH distribution of  $Q(v)$  and  $R(DT)$  the temperature difference as in  
541 equation (09). Assuming that the two distributions are independent, the combined distribution is the product of  $Q$   
542 and  $R$ . If we now define the variable  $z=v*DT$ , the new combined distribution on the heat flux variable  $z$  is given  
543 by the Mellin transform and convolution, described in Papoulis, A., & Pillai, S. U. (2002). The resulting  $P$   
544 distribution is an Asymmetric Laplace Distribution (ALD) like distribution which is similar to the one computed in  
545 Fig.4.

546



547 Figure A1: Histograms presenting the two original distributions,  $Q(v)$  (upper left quadrant, units wind speed) and  
548  $R(DT)$  (upper right quadrant, units degrees C) and the combined distribution for SH flux in units of  $W m^{-2}$ . The  
549 parameters used for the two original distributions are:  $k = 2.0$  for the Weibull shape,  $\lambda = 6.0$  for the Weibull  
550 scale;  $\alpha = -2.0$  for the Skew Normal shape,  $\mu = 2.0$  for the Skew Normal location and  $\omega = 2.5$  for the  
551 Skew Normal scale  
552

553  
554  
555  
556  
557  
558  
559  
560  
561  
562  
563  
564  
565  
566  
567  
568  
569  
570  
571  
572  
573  
574  
575  
576  
577  
578

## APPENDIX B

The statistical moments for the skew-normal PDF are given by:

$$E(x) = \mu + \lambda \delta \sqrt{\frac{2}{\pi}} \tag{B1}$$

$$\sigma^2 = \lambda^2 \left( 1 - \frac{2\delta^2}{\pi} \right) \tag{B2}$$

$$\mu_3 = (4 - \pi) \frac{(\delta \sqrt{2/\pi})^3}{2(1 - 2\delta^2/\pi)^{3/2}} \tag{B3}$$

$$\mu_4 = 2(\pi - 3) \frac{\left(\delta \sqrt{\frac{2}{\pi}}\right)^4}{\left(1 - \frac{2\delta^2}{\pi}\right)^2} \tag{B4}$$

where  $\delta = \frac{\alpha}{\sqrt{1 + \alpha^2}}$ . Since the expected value, E, of the time series is zero, we deduce that:

$$\mu = -\lambda \delta \sqrt{\frac{2}{\pi}} \tag{B5}$$

In other words, location and shape parameters have opposite signs since the scale parameter,  $\lambda$ , is always positive.

SH flux anomaly distribution was analysed with [the Asymmetric Laplace Distribution PDF](#), its statistical moments given by:

$$\text{mean} = \mu + \frac{1 - \alpha^2}{\lambda \alpha} \tag{B6}$$

$$\text{variance} = \frac{1 + \alpha^2}{\lambda^2 \alpha^2} \tag{B7}$$

$$\text{Skewness} = \frac{2(1 - \alpha^6)}{(\alpha^4 + 1)^{\frac{3}{2}}} \tag{B8}$$

$$\text{Kurtosis} = \frac{6(1 + \alpha^3)}{(1 + \alpha^4)^2} \tag{B9}$$

579 **References**

580

581 Azzalini, A.: A class of distributions which includes the normal ones. *Scandinavian journal of statistics*, 171-178,  
582 <https://www.jstor.org/stable/4615982>, 1985.

583

584 Bignami, F., S. Marullo, R. Santoleri, and M. E. Schiano.: Long wave radiation budget on the Mediterranean Sea,  
585 *J. Geophys. Res.*, 100, 2501–2514, <https://doi.org/10.1029/94JC02496>, 1995.

586

587 Bunker, A. F., H. Charnock, and R. A. Goldsmith.: A note on the heat balance of the Mediterranean and Red  
588 Seas, *Journal of Marine Research* 40, (S), [https://elischolar.library.yale.edu/journal\\_of\\_marine\\_research/1634](https://elischolar.library.yale.edu/journal_of_marine_research/1634),  
589 1982.

590

591 Béthoux, J. P.: Budgets of the Mediterranean Sea-Their dependance on the local climate and on the characteristics  
592 of the Atlantic waters. *Oceanologica acta*, 2(2), 157-163, 1979.

593

594 Béthoux, J. P., Gentili, B., & Tailliez, D.: Warming and freshwater budget change in the Mediterranean since the  
595 1940s, their possible relation to the greenhouse effect. *Geophysical Research Letters*, 25(7), 1023-  
596 1026, <https://doi.org/10.1029/98GL00724>, 1998.

597

598 Criado-Aldeanueva, F., Soto-Navarro, F. J., & García-Lafuente, J.: Seasonal and interannual variability of surface  
599 heat and freshwater fluxes in the Mediterranean Sea: Budgets and exchange through the Strait of Gibraltar,  
600 <https://dx.doi.org/https://doi.org/10.1002/joc.2268>, 2012.

601

602 Castellari, S., Pinardi, N., & Leaman, K.: A model study of air–sea interactions in the Mediterranean Sea. *Journal*  
603 *of Marine Systems*, 18(1-3), 89-114, [https://doi.org/10.1016/S0924-7963\(98\)90007-0](https://doi.org/10.1016/S0924-7963(98)90007-0), 1998.

604

605 Cessi, P., Pinardi, N. and Lyubartsev, V.: Energetics of semi enclosed basins with two-layer flows at the  
606 strait. *Journal of physical oceanography*, 44(3), pp.967-979, <https://doi.org/10.1175/JPO-D-13-0129.1>, 2014.

607

608 Cronin, M. F., Gentemann, C. L., Edson, J., Ueki, I., Bourassa, M., Brown, S., ... & Zhang, D.: Air-sea fluxes with  
609 a focus on heat and momentum. *Frontiers in Marine Science*, 6, 430, <https://doi.org/10.3389/fmars.2019.00430>,  
610 2019.

611

612 De Dominicis, M., Pinardi, N., Zodiatis, G., & Lardner, R. J. G. M. D.: MEDSLIK-II, a Lagrangian marine surface  
613 oil spill model for short-term forecasting–Part 1: Theory. *Geoscientific Model Development*, 6(6), 1851-1869,  
614 <https://doi.org/10.5194/gmd-6-1851-2013>, 2013.

615

616 Elderton, William Palin.: "Tables for Testing the Goodness of Fit of Theory to Observation". *Biometrika*. 1 (2):  
617 155–163, <https://www.jstor.org/stable/2331485>, 1902.

618

619 Escudier, R., Clementi, E., Cipollone, A., Pistoia, J., Drudi, M., Grandi, A., Lyubartsev, V., Lecci, R., Aydogdu, A.,  
620 Delrosso, D., Omar, M., Masina, S., Coppini, G., Pinardi, N.: A high-resolution reanalysis for the Mediterranean  
621 Sea. *Front. Earth Sci.* 9, 702285, <https://doi.org/10.3389/feart.2021.702285>, 2021.

622

623 Fairall, C. W., Bradley, E. F., Hare, J. E., Grachev, A. A., & Edson, J. B.: Bulk parameterization of air–sea fluxes:  
624 Updates and verification for the COARE algorithm. *Journal of climate*, 16(4), 571-591,  
625 [https://doi.org/10.1175/1520-0442\(2003\)016<0571:BPOASF>2.0.CO;2](https://doi.org/10.1175/1520-0442(2003)016<0571:BPOASF>2.0.CO;2), 2003.

626

627 Flecher, C., Naveau, P., Allard, D., & Brisson, N.: A stochastic daily weather generator for skewed data. *Water*  
628 *Resources Research*, 46(7), <https://doi.org/10.1029/2009WR008098>, 2010.

629

630 Garrett, C., Outerbridge, R., & Thompson, K.: Interannual variability in Mediterranean heat and buoyancy  
631 fluxes. *Journal of Climate*, 900-910, <https://www.jstor.org/stable/26197277>, 1993.

632

633 Gulev, S. K., & Belyaev, K.: Probability distribution characteristics for surface air–sea turbulent heat fluxes over  
634 the global ocean. *Journal of Climate*, 25(1), 184-206, <https://doi.org/10.1175/2011JCLI4211.1>, 2012.

635

636 Hersbach, H., Bell, B., Berrisford, P., Hirahara, S., Horányi, A., Muñoz-Sabater, J., ... & Thépaut, J. N.: The ERA5  
637 global reanalysis. *Quarterly Journal of the Royal Meteorological Society*, 146(730), 1999-2049, 2020.

638

639 Jordá, G., Von Schuckmann, K., Josey, S. A., Caniaux, G., García-Lafuente, J., Sammartino, S., ... & Macías, D.:  
640 The Mediterranean Sea heat and mass budgets: Estimates, uncertainties and perspectives. *Progress in*  
641 *Oceanography*, 156, 174-208, <https://doi.org/10.1016/j.pocean.2017.07.001>, 2017.

642

643 Korolev, V., Gorshenin, A., Gulev, S., & Belyaev, K.: Statistical modeling of air-sea turbulent heat fluxes by finite  
644 mixtures of Gaussian distributions. In *International Conference on Information Technologies and Mathematical*  
645 *Modelling* (pp. 152-162). Springer, Cham, [https://doi.org/10.1007/978-3-319-25861-4\\_13](https://doi.org/10.1007/978-3-319-25861-4_13), 2015.

646

647 Kara, A. B., Rochford, P. A., & Hurlburt, H. E.: Efficient and accurate bulk parameterizations of air–sea fluxes for  
648 use in general circulation models. *Journal of Atmospheric and Oceanic Technology*, 17(10), 1421-1438,  
649 [https://doi.org/10.1175/1520-0426\(2000\)017<1421:EAABPO>2.0.CO;2](https://doi.org/10.1175/1520-0426(2000)017<1421:EAABPO>2.0.CO;2), 2000.

650

651 Large, W., & Yeager, S. G.: The global climatology of an interannually varying air–sea flux data set. *Climate*  
652 *dynamics*, 33(2), 341-364, <https://doi.org/10.1007/s00382-008-0441-3>, 2009.

653

654 May, P. W.: A brief explanation of Mediterranean heat and momentum flux calculations, NORDA Code 322. *Nav*  
655 *Oceanogr Atmos Res Lab*, 5, 1986.

656

657 Marullo, S., Pitarch, J., Bellacicco, M., Sarra, A. G. D., Meloni, D., Monteleone, F., ... & Santoleri, R.: Air–sea  
658 interaction in the central Mediterranean Sea: assessment of reanalysis and satellite observations. *Remote*  
659 *Sensing*, 13(11), 2188.d; <https://doi.org/10.3390/rs13112188>, 2021.

660

661 Matsoukas, C., Banks, A. C., Hatzianastassiou, N., Pavlakis, K. G., Hatzidimitriou, D., Drakakis, E., ... & Vardavas,  
662 I.: Seasonal heat budget of the Mediterranean Sea. *Journal of Geophysical Research: Oceans*, 110(C12),  
663 <https://doi.org/10.1029/2004JC002566>, 2005.

664

665 Papoulis, A., & Pillai, S. U.: *Probability, Random Variables, and Stochastic Processes*, 4th Edition, 2002.

666

667 Payne, R. E.: Albedo of the sea surface. *Journal of Atmospheric Sciences*, 29(5), 959-970,  
668 [https://doi.org/10.1175/1520-0469\(1972\)029<0959:AOTSS>2.0.CO;2](https://doi.org/10.1175/1520-0469(1972)029<0959:AOTSS>2.0.CO;2), 1972.

669

670 Pettenuzzo, D., Large, W. G., & Pinardi, N.: On the corrections of ERA-40 surface flux products consistent with the  
671 Mediterranean heat and water budgets and the connection between basin surface total heat flux and NAO. *Journal*  
672 *of Geophysical Research: Oceans*, 115(C6), <https://doi.org/10.1029/2009JC005631>, 2010.

673

674 Pinardi, N., A. Bonaduce, A. Navarra, S. Dobricic, P. Oddo. The mean sea level equation and its application to the  
675 mediterranean sea. *J. Climate*, 27, 442–447, doi: 10.1175/JCLI-D-13-00139.1, 2014.

676

677 Pinardi, N., P. Cessi, F. Borile, and C.L. Wolfe.: [The Mediterranean Sea Overturning Circulation](https://doi.org/10.1175/JPO-D-18-0254.1). *J. Phys. Oceanogr.*,  
678 49, 1699–1721, <https://doi.org/10.1175/JPO-D-18-0254.1>, 2019.

679

680 Rabier, F., Järvinen, H., Klinker, E., Mahfouf, J. F., & Simmons, A.: The ECMWF operational implementation of  
681 four-dimensional variational assimilation. I: Experimental results with simplified physics. *Quarterly Journal of the*  
682 *Royal Meteorological Society*, 126(564), 1143-1170, <https://doi.org/10.1002/qj.49712656415>, 2000.

683

684 Rosati, A., and K. Miyakoda.: A general circulation model for upper ocean simulation, *J. Phys. Oceanogr.*, 18,  
685 1601–1626, [https://doi.org/10.1175/1520-0485\(1988\)018<1601:AGCMFU>2.0.CO;2](https://doi.org/10.1175/1520-0485(1988)018<1601:AGCMFU>2.0.CO;2), 1988.

686

687 Ruiz, S., Gomis, D., Sotillo, M. G., & Josey, S. A.: Characterization of surface heat fluxes in the Mediterranean Sea  
688 from a 44-year high-resolution atmospheric data set. *Global and Planetary Change*, 63(2-3), 258-274,  
689 <https://doi.org/10.1016/j.gloplacha.2007.12.002>, 2008.

690

691 [Reed, R. K.: On estimating insolation over the ocean. \*Journal of Physical Oceanography\*, 7\(3\), 482-485,](https://doi.org/10.1175/1520-0485(1977)007<0482:OEIOTO>2.0.CO;2)  
692 [https://doi.org/10.1175/1520-0485\(1977\)007<0482:OEIOTO>2.0.CO;2](https://doi.org/10.1175/1520-0485(1977)007<0482:OEIOTO>2.0.CO;2), 1977.

693

694 Small, R. J., Bryan, F. O., Bishop, S. P., & Tomas, R. A.: Air–sea turbulent heat fluxes in climate models and  
695 observational analyses: What drives their variability? *Journal of Climate*, 32(8), 2397-2421,  
696 <https://doi.org/10.1175/JCLI-D-18-0576.1>, 2019.

697

- 698 Sverdrup, H. U., Johnson, M. W., and Fleming, R. H.: The Oceans, Their Physics, Chemistry, and General Biology,  
699 Prentice-Hall, New York, <http://ark.cdlib.org/ark:/13030/kt167nb66r/>, 1942.  
700
- 701 Sanchez-Gomez, E., Somot, S., Josey, S. A., Dubois, C., Elguindi, N., & Déqué, M.: Evaluation of Mediterranean  
702 Sea water and heat budgets simulated by an ensemble of high-resolution regional climate models. *Climate*  
703 *dynamics*, 37(9), 2067-2086, <https://doi.org/10.1007/s00382-011-1012-6>, 2011.  
704
- 705 Song, X., & Yu, L.: Air-sea heat flux climatologies in the Mediterranean Sea: Surface energy balance and its  
706 consistency with ocean heat storage. *Journal of Geophysical Research: Oceans*, 122(5), 4068-4087,  
707 <https://doi.org/10.1002/2016JC012254>, 2017.  
708
- 709 Sardeshmukh, P. D., & Penland, C.: Understanding the distinctively skewed and heavy-tailed character of  
710 atmospheric and oceanic probability distributions. *Chaos: An Interdisciplinary Journal of Nonlinear Science*, 25(3),  
711 <https://doi.org/10.1063/1.4914169>, 2015.  
712
- 713 Tian, F., von Storch, J. S., & Hertwig, E.: Air-sea fluxes in a climate model using hourly coupling between the  
714 atmospheric and the oceanic components. *Climate Dynamics*, 48(9), 2819-2836, [https://doi.org/10.1007/s00382-](https://doi.org/10.1007/s00382-016-3228-y)  
715 [016-3228-y](https://doi.org/10.1007/s00382-016-3228-y), 2017.  
716
- 717 Tibshirani, R. J., & Efron, B.: An introduction to the bootstrap. *Monographs on statistics and applied*  
718 *probability*, 57(1), 1-436, 1993.  
719
- 720 Wallace, J. M., & Hobbs, P. V.: *Atmospheric science: an introductory survey* (Vol. 92), Elsevier, 2006.  
721
- 722 Yu, K., & Zhang, J.: A three-parameter asymmetric Laplace distribution and its extension. *Communications in*  
723 *Statistics—Theory and Methods*, 34(9-10), 1867-1879, <https://doi.org/10.1080/03610920500199018>, 2005.